Author: Nabuurs, Rob Johannes Antonius
Title: Molecular neuroimaging of Alzheimer's disease
Issue Date: 2014-05-28

Chapter 6

Detection of cortical changes in Alzheimer's disease at ultra-high field MRI

Submitted

Rob J.A. Nabuurs[#1]
Sanneke van Rooden[#1]
Sara van Duijn[2]
Maarten J. Versluis[1]
Bart J. Emmer[1]
Michael K. Liem[1]
Julien R. Milles[3]
Andrew G. Webb[1]
Matthew P. Frosch[4]
Sjoerd G. van Duinen[2]
Remco Natté[2]
Jeroen van der Grond[1]
Louise van der Weerd[1,5]
Mark A. van Buchem[1]

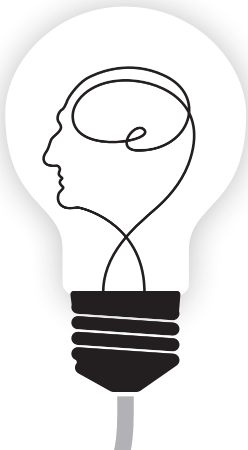

Abstract

Non-invasive methods to detect AD (AD) *in vivo* at an early stage are important for increasing our still incomplete understanding of the pathophysiology of the disease. Recently, 7T MRI systems that generate novel susceptibility-based contrasts in the human cerebral cortex have become available. In this study we aimed to assess whether differences in cortical appearance could be observed in AD patients using 7T MRI *in vivo* and to assess the nature of these changes by a histological-radiological correlation *ex vivo*.

In vivo regional cortical differences between probable AD patients (n=14) and healthy control subjects (n=15), visible on 7T susceptibility-weighted (SW) images, were analyzed after defining a novel scoring method based on the cortical appearance. In addition, post-mortem MRI of confirmed AD cases (n=6) was performed to assess the histological correlates of the changes observed *in vivo* in AD patients.

Diffuse hypointense bands were frequently found in the cortex of the frontal lobes of AD patients (57%), but not in controls. Histologic correlation revealed that the pattern of the susceptibility-weighted contrast in the cortex of AD patients does not primarily co-localize with amyloid plaques or neurofibrillary tangles, but with microglia- and myelin-associated iron accumulation and with an altered myelin cytoarchitecture.

Our observation of disturbed iron accumulation and myelin architecture in AD may have important implications for future *in vivo* diagnosis of AD, but also for the understanding of the pathophysiological mechanisms underlying this disease.

Introduction

For the definitive diagnosis of AD (AD) histological post-mortem detection of amyloid plaques and neurofibrillary tangles is required. During life, only a probable diagnosis can be made that is based primarily on clinical signs and symptoms.[1] However, recently it has been proposed to use biomarkers based on CSF analysis, structural MRI and amyloid imaging using PET, as supporting diagnostic criteria in research settings.[2]
Over the past few years, the feasibility of detecting the histological hallmarks of AD using MRI has been explored by many research groups. In general these efforts have focused on detecting individual amyloid plaques: increased iron accumulation around amyloid plaques induces a magnetic susceptibility effect, which is visible as hypointense foci on T_2*-weighted or susceptibility-weighted (SW) MRI in the cerebral cortex of transgenic AD mouse models and in human post-mortem brain slices.[3-5] However, these findings have not yet been convincingly replicated *in vivo* in patients, and it is doubtful whether detecting individual amyloid plaques with MRI will be possible in a clinical setting given the required high anatomical resolution, limited scanning time, and physiological motion of the patient. Furthermore, the central role of amyloid in the pathophysiology of AD remains a topic of debate. Although amyloid is still considered to be a hallmark as well as an initiating factor in the progression of the disease, there is increasing evidence that other primary or interacting causes, including changes in iron metabolism, may exist.[6,7]
Recent advances in human MRI systems operating at an ultra-high magnetic field strength (7 Tesla and higher) show that the increased sensitivity to susceptibility effects generates iron-based contrasts in the human brain that have not been observed at lower fields.[8] The aim of our study was to establish whether 7T MRI allows *in vivo* detection of differences in the cerebral cortex between probable AD patients and healthy age-matched controls. Having observed a difference, we then determined the histological substrate of the changes by comparing MRI to light- and electron microscopy (EM) of human post-mortem material of AD patients and controls.

Materials & Methods

In vivo **MRI study**

Participants

This study was approved by the institutional review board. In all cases, informed consent was obtained according to the declaration of Helsinki. Fourteen probable AD patients (mean age 76.4 years (range: 68 - 86), 9 males) and fifteen control subjects (mean age 75.1 years (range: 69 – 80), 10 males) were included. (**Table 1**) AD patients were recruited from the memory outpatient clinic of our institution. Memory outpatient clinic patients were referred to the hospital by their general practitioner or a medical specialist. Prior to the 7T MRI study these patients all underwent a routine clinical protocol, comprising a whole brain MRI (performed on a clinical 3 Tesla platform), a battery of neuropsychological tests, and a general medical and neurological examination performed by a neurologist, psychiatrist or internist-geriatrician. The diagnosis was made in a multidisciplinary consensus meeting using the National Institute of Neurological and Communicative Disorders and Stroke and AD and Related Disorders Association (NINCDS-ADRDA) criteria for diagnosing probable AD.[9] Participants with the diagnosis 'probable AD', who were capable of giving informed consent and who had a Mini Mental State Examination (MMSE) of ≥19 were selected for inclusion in the 7T study, either retrospectively within one year after attending the memory clinic, or prospectively. Healthy control subjects were recruited by focused advertisements. Subjects between 69 and 80 years of age, who were living independently and had an MMSE of ≥25 and a Geriatric Depression Scale (GDS) of ≤4 were selected for inclusion. Control subjects with the following diseases were excluded: stroke, Parkinson's disease, diabetes mellitus, rheumatoid arthritis, polymyalgia rheumatica, cancer, heart failure, and chronic obstructive pulmonary disease.

MRI data acquisition

Our study was performed on a human whole-body MRI system operating at a magnetic field strength of 7 Tesla (Philips Healthcare, Best, The Netherlands) using a quadrature transmit and 16-channel receive head coil (Nova Medical, Wilmington, MA, USA). AD-related pathology spreads throughout almost the entire brain, but macroscopically typically involves the fronto-temporal association cortices.[10-12] Participants were scanned using a 2D flow-compensated axial T_2*-weighted gradient-echo sequence which included the frontal lobe for detection of AD pathology with a total imaging duration of 10 minutes. Imaging parameters were: repetition time (TR)/echo time (TE) 794/25 ms, flip angle 45°, slice thickness 1.0 mm with a 0.1 mm interslice gap, 20 slices, 240 x 180 x 22 mm field of view, 1024x768 matrix size – resulting in an in-plane spatial resolution of 0.24 x 0.24 mm^2. The bandwidth per pixel was 46 Hz, corresponding to a readout length of approximately 22 ms. Frequency and phase encoding directions were along the anterior-posterior and right-left axes, respectively. This sequence is very sensitive to image artifacts arising from resonance frequency fluctuations within the brain caused by slight patient movements, even in areas significantly away from the head, and so a navigator echo was

Table 6.1 Characteristics of patients and controls and scoring results of the *in vivo* SWI study

	AD (n = 14)	Controls (n = 15)	p-value
Characteristics:			
Male / female	9 / 5	10 / 5	0.893
Mean age (range, yrs)	76.4 (68 - 86)	75.1 (69 - 80)	0.497
MSME (range)	22.5 (19 - 26)	29.2 (27 - 30)	0.000
Presence of diffuse band:			
Superior frontal lobe	2 / 14 (14.3%)	0 / 15 (0%)	0.224
Middle and inferior frontal lobe	8 / 14 (57.1%)	0 / 15 (0%)	0.001
Hypo-intense foci			
Superior frontal lobe	0 / 14 (0%)	0 / 14 (0%)	-
Middle and inferior frontal lobe	0 / 14 (0%)	0 / 14 (0%)	-

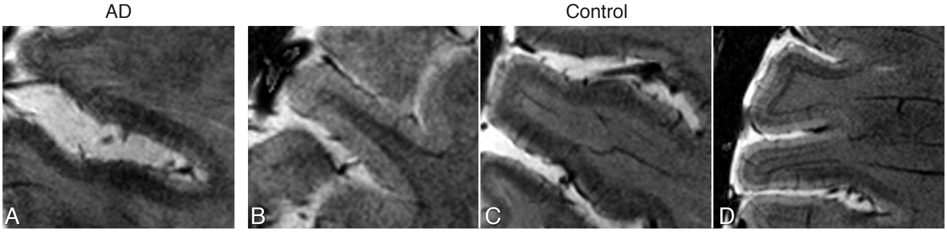

Figure 6.1 The observed variations of *in vivo* 7T SWI appearance of the human cortex
Shown are the middle/inferior frontal brain area of an AD patient (**A**) and healthy elderly controls (**B, C, D**). An clear example of a cortical ribbon containing a hypointense diffuse band is observed in the AD patient (**A**). Please note the blurring of the edges of the layers. (**B**) shows an example of a cortical ribbon containing one regular layer with higher signal intensity than the adjacent WM. In (**C**) a cortical ribbon is shown containing two well-defined layers. (**D**) shows a cortical ribbon containing three well-defined layers.

included to correct for these artifacts.[13] Shimming up to third order was performed using an image based shimming approach.[14] Phase images were unwrapped by high-pass filtering with a 92x92 kernel size. SW images were constructed by applying four phase mask multiplications.[15] Whole brain imaging at this high spatial resolution (0.24 x 0.24 x 1 mm^3) however would result in an impractically long imaging duration, particularly for AD patients.[13] Since susceptibility artifacts induced by the temporal bone hampered the imaging of the temporal lobe, the final imaging volume focused on the frontal lobe, which is less prone to atrophy than the temporal lobe, but is known to accumulate high amyloid loads[16], to have a lower metabolic rate[17], and to have an altered resting state network connectivity in AD.[18]

Image analysis

Based on previous 7T MRI studies of the human cortex in post-mortem brain specimens of AD patients[4] and *in vivo* imaging of healthy volunteers[19] we developed a scoring method to capture the appearance of the cortex on SW images. We defined a normal cortex based on the following criteria: **a)** a cortical ribbon containing one homogeneous layer with a higher signal intensity as compared to the adjacent white matter (WM), **b)** a cortical ribbon containing two well-defined, homogeneous layers, with the superficial layer demonstrating a higher signal intensity compared to the deepest layer (the layer adjacent to the WM) and the WM, or **c)** a cortical ribbon with three layers: the same layers as previously described separated by a third thin layer with a lower signal intensity than the other two layers. (**Figure 6.1**) Abnormal cortex was classified as a deviation from the normal patterns described above, showing the presence of well-defined foci of signal loss (hypointense foci) and/or more diffuse areas with lower signal intensity in the superficial layer as compared to the adjacent WM (a diffuse band). (**Figure 6.1**) Features were scored as present or absent per subject in several predefined gyri of the frontal lobe. (**Table 6.1**) Uniform window settings were used for all images. Images were scored by two neuroradiologists (B.E. and M.L.) who were blinded for the diagnosis in a consensus reading.

Statistics

A Mann-Whitney U-test was used to assess differences in age and MMSE, and a chi-square test was used to assess differences in gender between AD and control groups. For each feature

Table 6.2 Post-mortem subject characteristics and SWI analysis

Subject characteristics						9.4 T SWI analysis			
No.	Age / Sex	Diagnose	Cause(s) of death	Braak	Amyloid	Homogenous with cortical layers	Diffuse band	Hypo-intense foci	Clouds
1	83 / F	Control	Arrhythmia	II	0	Yes	-	-	-
2	93 / F	Control	Acute death	I	A	Yes	-	-	-
3	89 / F	Control	Myocardial infarct / Pneumonia	III	A	No	+	+	+
4	77 / M	AD	Cachexia / dehydration by advanced dementia syndrome	VI	C	No	+	+	-
5	85 / F	AD	Aspiration pneunomia by advanced dementia syndrome	IV	C	No	+	-	+
6	87 / F	AD	Respiratory tract infection / cerebrovascular accident	VI	C	No	+	-	+
7	87 / M	AD	Cachexia / dehydration by advanced dementia syndrome	V	C	No	+	+	-
8	87 / F	AD	Sepsis	V	C	No	-	-	+
9	88 / F	AD	Unknown	IV	C	No	+	-	+

Characteristics are based on clinical information and standard neuropathologic examination according to the Braak criteria for tau and amyloid pathology.[20] The scoring indicates the presence (+) or absence (-) of the different patterns on the corresponding SW images. *F = female; M = male.*

(hypointense foci and/or a diffuse band), a Fisher's exact test was performed per brain region. Positive and negative predictive values of the features to detect AD were calculated per brain region. All statistical analyses were performed with the Statistical Package of Social Sciences (SPSS 17.0.1; SPSS, Chicago, Ill).

Post-mortem MRI study

Study design

To investigate the histological substrates responsible for the observed *in vivo* MRI changes at 7T, we applied similar scan methods on post-mortem material of AD patients and controls using a vertical-bore 9.4 T system (Bruker Biospin, Ettlingen, Germany). For each sample high-resolution (isotropic 40 μm voxels) images were acquired, as well as images with a similar resolution (isotropic 200 μm voxels) as were used in the *in vivo* study. The lower resolution MR images were acquired to help translation between the *in vivo* and *ex vivo* MR data sets. The high-resolution MR images helped to identify the particular MR images that matched best with the 8-μm thick histological sections.

Sample preparation

Brain tissue was obtained from the tissue bank of the Department of Pathology at our institution and from the Netherlands Brain Bank (NBB, Netherlands Institute for Neuroscience, Amsterdam). Following a post-mortem interval of <19 hours, brains were resected and stored in 4% paraformaldehyde. At both institutions brain tissue was examined histologically for the presence of AD-related pathology and scored using the Braak classification.[20] Based on availability six samples with a clinical diagnosis of AD by histological confirmation were selected, as well as three age-matched non-demented controls. (**Table 6.2**) Patient anonymity was strictly maintained. All tissue samples were handled in a coded fashion, according to Dutch national ethical guidelines (Code for Proper Secondary Use of Human Tissue, Dutch Federation of Medical Scientific Societies). To avoid formalin-induced artifacts in the MR images only material fixed for a period of between three months and two years was used.[21] From each subject one tissue block of approximately 4 x 15 x 15 mm^3 was resected from the medial temporal lobe using a vibratome (VT1000S, Leica, Germany). Care was taken to ensure that the samples were resected with a similar gyral orientation. Residual formalin was washed out by placing the samples in phosphate buffered saline (PBS) for >24 hours to partially restore MR relaxation parameters.[22] For MRI, each sample was placed in a customized tissue container and immersed in a proton-free fluid (Fomblin LC08, Solvay). Air was removed by application of a vacuum for several minutes.[21]

Post-mortem MRI

Scans were acquired on a 9.4 Tesla vertical bore MRI system, equipped with a 1 T/m actively-shielded gradient insert and Paravision 5.0 imaging software (Bruker Biospin, Ettlingen, Germany). A 20-mm diameter birdcage transmit/receive coil was used to acquire T_2*-weighted 3D gradient echo images with TR = 75 ms; TE = 22.5 ms; flip angle = 25° at either 200 μm isotropic resolution with 20 signal averages, or 40 μm isotropic resolution with 28 signal averages. The average scan time per resolution was approximately 40 minutes (200 μm resolution) or 25 hours (40 μm resolution), with minor differences between samples of slightly different sizes. To create SW images comparable to *in vivo* scans, the 200 μm resolution phase images were unwrapped using a k-space Hanning filter with a width set to 50% of the image size.[23] Final SW images were reconstructed from the original images by four phase mask multiplications.[15] All data processing was performed with MatLab (MathWorks, Natick, MA).

Post-mortem image analysis

For assessment of *ex vivo* SW images we used the same criteria as were used *in vivo* for defining normal and abnormal cortex (hypointense bands and hypointense foci). In addition, since the *ex vivo* images showed increased anatomical detail compared to the *in vivo* scans (due to the absence of physiological motion), a third category of abnormal cortex could be added, namely diffuse areas with low signal intensity, not extending parallel to the cortical surface (as in healthy tissue) but instead expanding locally in an irregular fashion throughout the cortex, a feature which we have termed "clouds" (**Suppl. Figure 6.1**). Window settings were optimized for each sample based on the WM and gray matter (GM) histogram. The 200 μm SW images were scored blinded for diagnosis by a neuroradiologist (M.v.B) and MR-microscopy expert (L.v.d.W) in a consensus reading.

Histology and electron microscopy

All brain samples were paraffin-embedded and serially cut into 8-μm thick sections. Tissue morphology was assessed by standard hematoxylin-eosin (HE) staining. Iron was detected using a 3'3-diaminobenzidine-tetrahydrochloride (DAB) enhanced Perls' staining protocol for light microscopy and EM which has shown to be the most sensitive to detect iron-positive structures in paraffin-embedded human AD brain tissue.[24,25] Consecutive sections were (co-)stained for amyloid-beta (Aβ), paired helical filament-tau (AT8), myelin (protolipid-protein (PLP)), microglia (CD68 and HLA-DR) and activated astrocytes (GFAP). (**Suppl. Table 6.1**) Endogenous peroxidase was blocked by 30 minutes of incubation in methanol with 0.02% H_2O_2. After these pre-treatments, non-specific binding was minimized by incubation with 10% fetal calf serum (DakoCytomation). Labeling was visualized by DAB staining (DakoCytomation). All sections were digitized with a microscope scanner (Panoramic, 3DHistotech, Hungary) for global and microscopic evaluation. To assess co-localization of cellular iron with CD68, HLA-DR or GFAP-positive cells, sections stained for iron as described above were subsequently treated according to the previously described immunohistochemical procedures except for using an Alexa647-labeled secondary anti-mouse antibody for immunofluorescence. (**Suppl. Table 6.1**) Co-localization of these antigens with iron was assessed using a confocal fluorescence microscope (LSM 510, Zeiss, Germany). Iron-stained ultrathin (100 nm) sections were examined by electron microscopy (JEM-1011, JEOL, Germany) to assess the exact localization of the cortical iron in the neuropil.

Histology-MRI correlation

The digitized histological sections were matched with their corresponding high-resolution (40 μm) MR images by visual comparison of the contour and vascular architecture of each section. The corresponding low-resolution SW image that matched best with the histological section could then be identified directly since the two SW image datasets are inherently co-registered. To assess the histological substrate of the cortical changes observed on MR images, the digitized histological sections were first inspected at low magnification (2x) alongside the corresponding low-resolution SW image. Subsequently, these areas were further analyzed microscopically at higher magnification (40x) to look for the microscopic changes underlying the MR. All observations were independently verified by three neuropathologists (R.N., S.v.D., M.F.).

Results

The characteristics of the participants for *in vivo* MRI are shown in **Table 6.1**. No difference in age (p = 0.497) or gender (p = 0.893) was found between patient and control groups. Scores for global cognitive functioning (MMSE score) were significantly higher in controls (29.2 points; range 27-30) than in patients with AD (22.5 points, range 19-26), p<0.001. 7T SW images of the frontal lobe of probable AD patients (n=14) were visually compared to those of control subjects (n=15).

We developed a scoring method to rate the cortical appearance based on previous 7T observations in normal brain and post-mortem observations in AD patients, distinguishing normal-appearing cortical patterns with one or more homogeneous layers from hypo-intense foci or hypointense diffuse bands. (**Figure 6.1**) Clear *in vivo* differences between AD patients and controls were seen in terms of the presence of diffuse hypointense bands on the SW images. (**Table 6.1** and **Figure 6.2**)

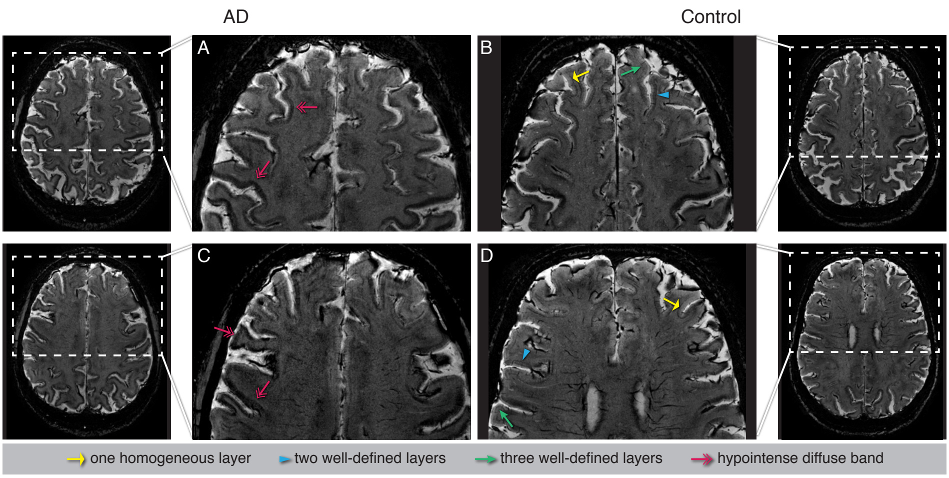

Figure 6.2 ***In vivo*** **cortical differences seen on SWI in AD patients versus age-matched control subjects**
Regional distribution of the observed variations of *in vivo* 7T SWI appearance as presented in Figure 6.1, shown in an AD patient and a control subject. The left two columns (**A** and **C**) show an AD patient and the right two columns (**B** and **D**) a control subject. The upper row (**A** and **B**) shows the superior frontal region, the lower row (C and D) the middle and inferior frontal region. In the AD patient a diffuse band is seen in both regions of the frontal lobe and *the double arrows* show several locations containing this band whereas in the control subject this diffuse band is absent and a regular layer (*arrow*), two-well defined layers (*arrowhead*) and three-well defined layers (*small arrow*) could be detected.

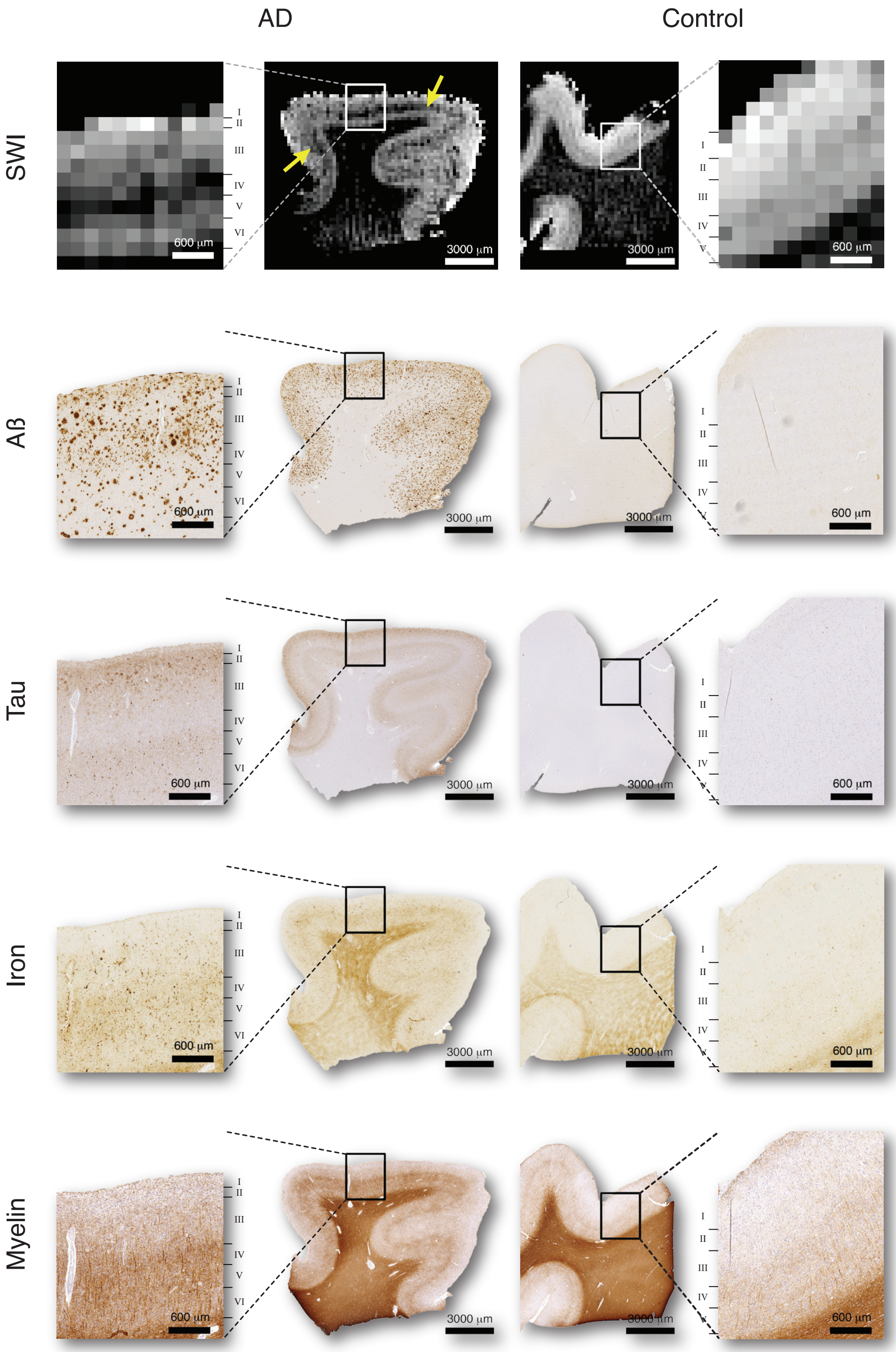
AD
Control
SWI
Aß
Tau
Iron
Myelin
I
II
III
IV
V
VI
600 µm
3000 µm

Figure 6.3 Comparison of post-mortem SWI with histology
The SWI image of the AD patient (Table 6.2 subject 7) showed a midcortical hypointense band (*yellow arrows*) in addition to several focal hypo-intensities, as opposed to a clear homogenous cortex as seen in the control subject (Table 6.2 subject 1). For detailed evaluation similar regions of interest of the cortex are shown alongside each corresponding main image and the cortical layers have been assigned accordingly. Neither the cortical distribution of Aβ or tau matched the hypointense band. Tau typically showed a band-like pattern in cortical layers II – III and V, and so is not co-localized in the layer corresponding to MR signal decrease. Both iron and myelin correlated with the observed pattern of band-like hypo-intensities, including a diminished staining in the inner cortical layers V and VI. As compared to the control, the iron staining of the AD subject showed an increase in cellular deposits and diffuse iron within the neuropil, mainly centered around cortical layer IV spreading to both sides with overlap in layers III and IV. The myelin distribution visualized by the PLP-immunostaining showed a similar pattern of increased staining in the AD subject resulting from a denser network of thin myelinated fibers. Similar to previous reports, in the AD patient the cortex also contained several small roundish areas devoid of myelinated fibers suggesting the presence of amyloid plaques based on their morphological appearance.[29]

Within the frontal lobe, these patterns were found in the middle and inferior frontal gyri in eight out of 14 patients, whereas these diffuse bands were not observed in any of the control subjects. In these frontal gyri, the diffuse hypointense band was significantly more prevalent in AD patients as compared to controls ($p = 0.001$), with positive predictive and negative values of 100% and 71%, respectively. In the superior frontal gyrus, a similar hypointense band was observed in only two out of the 14 AD patients and in none of the control subjects: there was no significant difference between the two groups ($p = 0.224$). For this specific cortical region, corresponding positive and negative predictive values were 100% and 55%, respectively. Foci of signal loss were not observed in the frontal lobe in either AD patients or control subjects.
Post-mortem cerebral cortex samples of six AD cases and three age-matched controls were scanned with a similar SWI protocol as for the *in vivo* MRI. Two of the controls showed a normal cortex. The control subject with an abnormal cortex revealed AD-type pathology (Braak stage III), despite the absence of an ante-mortem clinical AD diagnosis. We therefore discuss the findings in this case separately.

In all post-mortem AD samples (six out of six), an abnormal cortex was observed on SW images. (**Table 6.2**) Hypointense bands were observed in five out of six AD cases, and in the control with Braak III. Due to the lack of physiological movements, the *ex vivo* images that were acquired with a similar resolution as the *in vivo* images provided more anatomical detail, and demonstrated that the hypointense bands did not cover the full width of the cortex, but were located centrally in the cortex. (**Figure 6.3**) Hypointense foci were observed in two out of six AD cases, and in the one control specimen with Braak III. In addition to the scoring criteria defined for the *in vivo* scans, in these post-mortem samples a third category of cortical disturbance could be observed, consisting of cloud-like areas of low signal intensity with less alignment along, and more expansion through, the cortical layers (four out of six AD cases, and in the control subject with Braak III). (**Suppl. Figure 6.1**)

Comparing radiological and histological data of the same sample, the epicenter of the hypointense bands and clouds observed on the *ex vivo* MR images could be localized in cortical layer IV. Subsequently, we assessed which of the histological markers (Aβ, tau, iron, and myelin) showed a similar distribution over the cortical layers to the hypointense bands and clouds. We observed that the hypointense bands and clouds on MRI co-localized with areas characterized by an increased presence of iron and changes in myelin structure. (**Figure 6.3**)

Only cortices that were scored as abnormal on SW images demonstrated these accentuated local patterns for iron and myelin on histological examination. Interestingly, no co-localization was observed between the hypointense bands and clouds on MRI and areas staining for Aβ or tau. Tau pathology typically affected cortical layers II – III and V. Aβ staining was present to an equal extent across all cortical layers. Microscopically, some of the hypointense foci observed on the *ex vivo* images corresponded to large amyloid plaques, but these focal signal voids barely contributed to the observed hypointense cortical bands. (**Suppl. Figure 6.2**)
Since the pattern of the abnormalities observed on MRI corresponded best with the patterns observed on iron and myelin-stained tissue, we examined these stainings in more detail. Microscopically, using higher magnification, four different types of iron accumulation were observed in the cortex: 1) diffuse neuropil deposition associated with myelinated fibers, 2) dense stellate cytoplasmic iron accumulation in microglial cells, 3) a dense thin line of perinuclear iron accumulation in oligodendroglial and microglial cells, and 4) iron associated with amyloid plaques. (**Figure 6.4**)

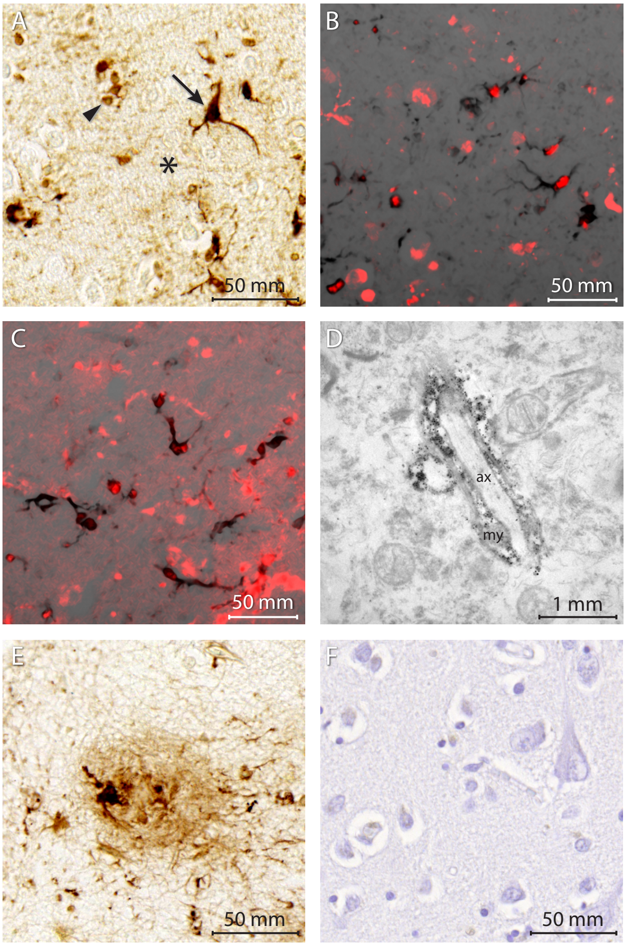

Figure 6.4 Characterization of intracortical iron distribution in AD brain tissue
Shown are the different types of cellular and neuropilar intracortical iron in the medial temporal lobe of an AD patient (Table 6.2 subject 7). (**A**) Indicated by the brown color due to the modified 3'3-DAB enhanced Perls' iron staining, iron is present as perinuclear (*arrow head*) and stellate cellular deposits (*arrow*), and as diffuse iron spread throughout the neuropil (*asterix*). Morphologically the cellular iron was attributed to oligodendro- or microglia cells. The latter was further verified by the co-localization of iron (black) with (**B**) CD68 (*red*) and (**C**) HLA-DR (*red*) immunostaining. As indicated by both stainings, even in close proximity to these iron-bearing microglia, several microglia were present that were completely devoid of iron. (**D**) Ultrastructurally, as shown by EM, neuropil iron was found to be located in the myelin sheets folded around an axon. (**E**) A example of iron found associated with an amyloid plaque. (**F**) The negative iron staining of a consecutive section did not result in any DAB enhancement, thereby confirming specificity of the iron stain. (*axon, ax; myelin sheet, my*)

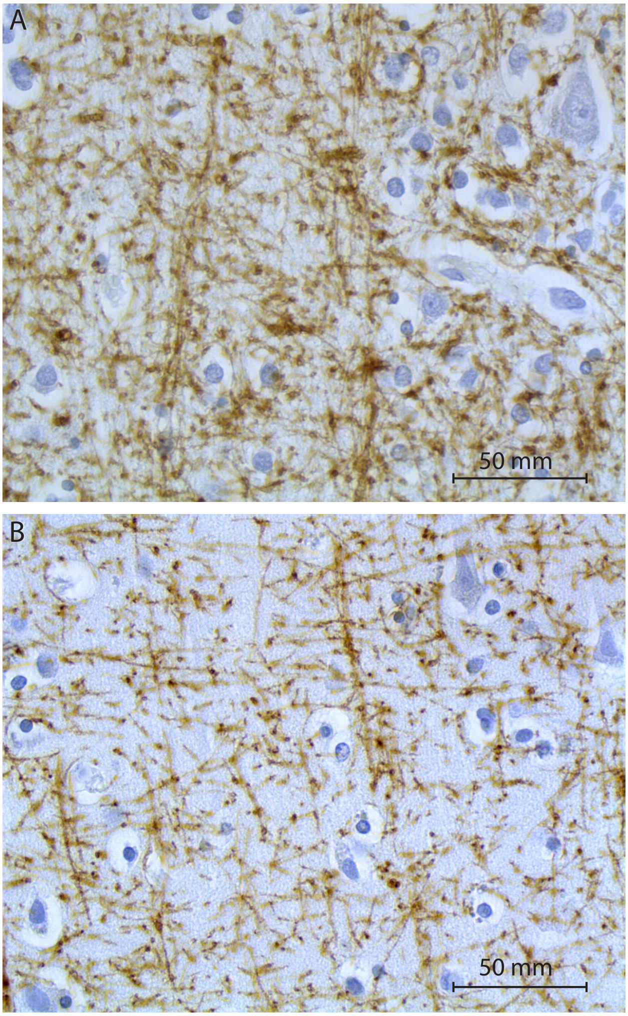

Figure 6.5 Structural alterations of intracortical myelin
In addition to the observed differences in myelin highlighted by Figure 6.3, this figure presents a more detailed comparison of the intracortical myelin of the medial temporal lobe of (**A**) an AD patient (Table 6.2 subject 4) and (**B**) a non-demented age-matched control (Table 6.2 subject 1). Shown are midcortical regions (layer IV) with a comparable orientation assessed by a PLP-immunostaining (*brown*). At this higher magnification, the intracortical myelin in the AD subjects was characterized by an accentuated PLP staining due to changes in myelin structure comprising fragmentation, increased segmental tortuosity and bead-like varicosities. As a result the PLP staining of the AD cortex appeared disorganized with loss of individually discernable fibers and orientation when compared to the cortex of the control subjects.

All four types of iron deposits were more abundant in the subjects with an abnormally appearing cortex on post-mortem MRI, including the control subject with Braak III. The first three types of iron deposits were localized differently in the cortical layers: neuropil iron accumulation was centered in layer IV, extending into layers III and V of the cortex; stellate glial aggregates were most abundant in the middle cortical layers (layers III and IV), but were also present to a lesser extent in the deep cortical layers (layers V and VI), and perinuclear glial iron accumulation was most abundant in layers V and VI, followed by layers IV and III. (**Figure 6.3**) In addition, increased microglial and neuropil iron accumulations were also observed in areas characterized by cloud-like hypo-intensities on MRI. EM analysis revealed that the diffuse iron in the neuropil was located predominantly in oligodendrocytic myelin sheaths. (**Figure 6.4D**)
The association of iron with myelin sheaths in the neuropil led us to examine the cortical myelin in more detail using a PLP staining. Interestingly, the intensity of myelin staining also showed a

colocalization with the low signal intensity bands and clouds on MRI. (**Figure 6.3**) Histologically, these areas were characterized by an accentuated PLP staining due to changes in myelin structure comprising fragmentation, increased segmental tortuosity and bead-like varicosities, centralized in layer IV, but extending to layers III and V in the AD patients. (**Figure 6.3** and **6.5**) Furthermore, as expected, small round plaque-like areas that were devoid of any myelin fibers were observed in cortical areas containing a high number of Aβ deposits.

Discussion

Using 7T MRI we observed striking differences *in vivo* in the frontal cortex between AD patients and age-matched controls. In patients with probable AD we found a disturbance of the layered structure of the cortex. Previous studies in healthy subjects demonstrated that cortical lamination at 7T reflects intracortical myeloarchitecture[8,19,26], and this normal pattern of cortical lamination was attributed to differences in myelin-associated iron and myelin lipids in the different cortical layers.[19] Our current study shows that in AD patients the cortical areas of altered SW contrast co-localize with areas of increased microglia- and myelin-associated iron accumulation and also with changes in myelin cytoarchitecture. However, our data also demonstrate that the pattern of the changes observed on MRI does not correspond to the pattern of amyloid deposits. These observations are not in line with the previous assumption, mostly based on animal experiments, that T_2*-weighted and SW imaging contrast in AD primarily reflects the presence of iron associated with amyloid plaques.[3-5,19] Our observations of disturbed iron accumulation and myelin architecture have important implications for *in vivo* diagnosis of AD, and also for the understanding of the pathophysiological mechanisms underlying this disease.

According to the amyloid hypothesis oligomeric forms of Aβ are the trigger for a cascade of events that ultimately results in dementia. However, there is increasing evidence that a range of other etiological factors have an important impact on this cascade, presumably by interacting with the Aβ aggregates or by subsequent cellular changes which follow it.[6,11,27] In our study, we found a close correlation between SW MRI contrast changes, myelin changes and increased iron accumulation in cortices with AD pathology. Interestingly, changes in iron metabolism and myelin breakdown have both been mentioned as potential upstream mechanisms for AD.[11,27]

Iron and myelin are closely associated in the brain. Seventy percent of the brain's iron is located in oligodendrocytes. Maturation of oligodendrocytes and myelin synthesis are both dependent on the availability of iron.[11,28] During demyelination processes in disease, as well as during normal myelin turnover, iron is assumed to be released from myelin into the brain tissue.[11] Our observation of increased iron in microglial cells (which have an important phagocytic role) in areas of altered myelin structure suggests that the observed MRI changes are a reflection of increased demyelination.

Cortical demyelination has been observed previously in AD, but mainly as areas of focal myelin loss in the immediate vicinity of amyloid plaques.[29,30] We also observed this pattern of myelin loss in our samples, but it was much less prominent than the more diffuse changes in myelin structure (increased fragmentation, tortuosity, and bead-like varicosities) which we report here.

To our knowledge, these findings have not been reported before in human AD, but strikingly similar myelin alterations were recently discovered in a mouse model of AD.[31]

Apart from its role in myelin metabolism, iron is an important upstream and downstream modulator of several molecular pathways in AD. Recently it was demonstrated that APP plays a physiological role in preventing iron-mediated oxidative stress in the brain.[32] In AD, zinc accumulation in amyloid plaques and loss of soluble tau interfere with APP's ferroxidase activity, causing increased neuronal iron accumulation. Furthermore, there is evidence that APP processing through the amyloidogenic and non-amyloidogenic pathways is affected by iron.[32,33] Finally, experimental data have demonstrated that iron may accelerate Aβ oligomerization.[34] Based on these observations, it has been suggested that iron could be an important biomarker of AD.[35,36]

The data presented here show convincing evidence that the cortical myelin cytoarchitecture and iron distribution are disturbed in AD patients. Although these changes might not be central to the pathogenesis of AD, the ability to visualize them by MRI creates a putative novel biomarker with the potential to reflect an as yet underappreciated change that may accompany the progression of AD. However, our data are preliminary since they have been generated in a limited number of patients and healthy controls, and cover only a limited part of the brain. Post-mortem, we observed these changes in SWI contrast in all patients with confirmed AD. *In vivo*, we observed these changes in cortical appearance only in a sub-set of patients; one reason for this discrepancy may be that the patients have been included based on a clinical diagnosis (NINCDS-ADRDA criteria), which is known to have a limited diagnostic accuracy (77 - 85%).[37] Further studies, comprising larger patient series and additional controls populations of patients with different types of dementia are required to assess the potential of the cortical changes we observed to constitute true diagnostic biomarkers for AD. There are many other important and related questions, such as whether the presence of cortical changes is associated with reduced cognitive function, whether the changes appear early in the course of AD, and whether the frontal lobes are the best regions in which to detect these early changes. Additional *in vivo* and post-mortem research on the correlation between ultra-high field MRI and pathology will allow us to further elucidate the role of iron and myelin in the pathogenesis of AD. Overall, the analysis of the cortical changes via visual inspection and simple scoring criteria, without the need for quantitative measurements or sophisticated image processing techniques, makes the proposed method very attractive as a diagnostic and research tool in a clinical setting.

References

1. Montine, TJ, Phelps, CH, Beach, TG, *et al*. National Institute on Aging-Alzheimer's Association guidelines for the neuropathologic assessment of AD: a practical approach. Acta Neuropathol. 2012; 123:1-11.
2. Jack, CR, Jr., Knopman, DS, Jagust, WJ, *et al*. Hypothetical model of dynamic biomarkers of the Alzheimer's pathological cascade. Lancet Neurol. 2010; 9:119-128.
3. Chamberlain, R, Wengenack, TM, Poduslo, JF, *et al*. Magnetic resonance imaging of amyloid plaques in transgenic mouse models of AD. Curr Med Imaging Rev. 2011; 7:3-7.
4. van Rooden, S, Maat-Schieman, ML, Nabuurs, RJ, *et al*. Cerebral amyloidosis: post-mortem detection with human 7.0-T MR imaging system. Radiology. 2009; 253:788-796.
5. Meadowcroft, MD, Connor, JR, Smith, MB, *et al*. MRI and histological analysis of beta-amyloid plaques in both human AD and APP/PS1 transgenic mice. J Magn Reson Imaging. 2009; 29:997-1007.
6. Fjell, AM and Walhovd, KB. Neuroimaging results impose new views on AD--the role of amyloid revised. Mol Neurobiol. 2012; 45:153-172.
7. Karran, E, Mercken, M, and De, SB. The amyloid cascade hypothesis for AD: an appraisal for the development of therapeutics. Nat Rev Drug Discov. 2011; 10:698-712.
8. Fukunaga, M, Li, TQ, van, GP, *et al*. Layer-specific variation of iron content in cerebral cortex as a source of MRI contrast. Proc Natl Acad Sci U S A. 2010; 107:3834-3839.
9. McKhann, G, Drachman, D, Folstein, M, *et al*. Clinical diagnosis of AD: report of the NINCDS-ADRDA Work Group under the auspices of Department of Health and Human Services Task Force on AD. Neurology. 1984; 34:939-944.
10. Alves, L, Correia, AS, Miguel, R, *et al*. AD: a clinical practice-oriented review. Front Neurol. 2012; 3:63.
11. Bartzokis, G. AD as homeostatic responses to age-related myelin breakdown. Neurobiol Aging. 2011; 32:1341-1371.
12. Duyckaerts, C, Delatour, B, and Potier, MC. Classification and basic pathology of Alzheimer disease. Acta Neuropathol. 2009; 118:5-36.
13. Versluis, MJ, Peeters, JM, van Rooden, S, *et al*. Origin and reduction of motion and f0 artifacts in high resolution T2*-weighted magnetic resonance imaging: application in AD patients. Neuroimage. 2010; 51:1082-1088.
14. Schar, M, Kozerke, S, Fischer, SE, *et al*. Cardiac SSFP imaging at 3 Tesla. Magn Reson Med. 2004; 51:799-806.
15. Haacke, EM, Xu, Y, Cheng, YC, *et al*. Susceptibility weighted imaging (SWI). Magn Reson Med. 2004; 52:612-618.
16. Rowe, CC and Villemagne, VL. Brain Amyloid Imaging. J Nucl Med. 2011.
17. Langbaum, JB, Chen, K, Lee, W, *et al*. Categorical and correlational analyses of baseline fluorodeoxyglucose positron emission tomography images from the AD Neuroimaging Initiative (ADNI). Neuroimage. 2009; 45:1107-1116.
18. Rombouts, SA, Barkhof, F, Goekoop, R, *et al*. Altered resting state networks in mild cognitive impairment and mild AD: an fMRI study. Hum Brain Mapp. 2005; 26:231-239.
19. Duyn, JH, van, GP, Li, TQ, *et al*. High-field MRI of brain cortical substructure based on signal phase. Proc Natl Acad Sci U S A. 2007; 104:11796-11801.
20. Braak, H, Alafuzoff, I, Arzberger, T, *et al*. Staging of Alzheimer disease-associated neurofibrillary pathology using paraffin sections and immunocytochemistry. Acta Neuropathol. 2006; 112:389-404.
21. van Duijn, S, Nabuurs, RJ, van, RS, *et al*. MRI artifacts in human brain tissue after prolonged formalin storage. Magn Reson Med. 2011.
22. Shepherd, TM, Thelwall, PE, Stanisz, GJ, *et al*. Aldehyde fixative solutions alter the water relaxation and diffusion properties of nervous tissue. Magn Reson Med. 2009; 62:26-34.
23. Wang, Y, Yu, Y, Li, D, *et al*. Artery and vein separation using susceptibility-dependent phase in contrast-enhanced MRA. J Magn Reson Imaging. 2000; 12:661-670.
24. Meguro, R, Asano, Y, Odagiri, S, *et al*. Nonheme-iron histochemistry for light and electron microscopy: a historical, theoretical and technical review. Arch Histol Cytol. 2007; 70:1-19.
25. van Duijn, S, Nabuurs, RJ, van Duinen, SG, *et al*. Comparison of histological techniques to visualize iron in paraffin-embedded brain tissue of patients with AD. J Histochem Cytochem. 2013; 61:785-792.
26. Cohen-Adad, J, Polimeni, JR, Helmer, KG, *et al*. T(2)* mapping and B(0) orientation-dependence at 7 T reveal cyto- and myeloarchitecture organization of the human cortex. Neuroimage. 2012; 60:1006-1014.
27. Herrup, K. Reimagining AD--an age-based hypothesis. J Neurosci. 2010; 30:16755-16762.
28. Todorich, B, Pasquini, JM, Garcia, CI, *et al*. Oligodendrocytes and myelination: the role of iron. Glia. 2009; 57:467-478.

29. Mitew, S, Kirkcaldie, MT, Halliday, GM, *et al*. Focal demyelination in AD and transgenic mouse models. Acta Neuropathol. 2010; 119:567-577.
30. Serrano-Pozo, A, William, CM, Ferrer, I, *et al*. Beneficial effect of human anti-amyloid-beta active immunization on neurite morphology and tau pathology. Brain. 2010; 133:1312-1327.
31. Chen, H, Epelbaum, S, and Delatour, B. Fiber Tracts Anomalies in APPxPS1 Transgenic Mice Modeling AD. J Aging Res. 2011; 2011:281274.
32. Duce, JA, Tsatsanis, A, Cater, MA, *et al*. Iron-export ferroxidase activity of beta-amyloid precursor protein is inhibited by zinc in AD. Cell. 2010; 142:857-867.
33. Lei, P, Ayton, S, Finkelstein, DI, *et al*. Tau deficiency induces parkinsonism with dementia by impairing APP-mediated iron export. Nat Med. 2012; 18:291-295.
34. Roberts, BR, Ryan, TM, Bush, AI, *et al*. The role of metallobiology and amyloid-beta peptides in AD. J Neurochem. 2012; 120 Suppl 1:149-166.
35. Collingwood, J and Dobson, J. Mapping and characterization of iron compounds in Alzheimer's tissue. J Alzheimers Dis. 2006; 10:215-222.
36. Zhu, WZ, Zhong, WD, Wang, W, *et al*. Quantitative MR phase-corrected imaging to investigate increased brain iron deposition of patients with Alzheimer disease. Radiology. 2009; 253:497-504.
37. Jobst, KA, Barnetson, LP, and Shepstone, BJ. Accurate prediction of histologically confirmed AD and the differential diagnosis of dementia: the use of NINCDS-ADRDA and DSM-III-R criteria, SPECT, X-ray CT, and Apo E4 in medial temporal lobe dementias. Oxford Project to Investigate Memory and Aging. Int Psychogeriatr. 1998; 10:271-302.
38. Natte, R, Maat-Schieman, ML, Haan, J, *et al*. Dementia in hereditary cerebral hemorrhage with amyloidosis-Dutch type is associated with cerebral amyloid angiopathy but is independent of plaques and neurofibrillary tangles. Ann Neurol. 2001; 50:765-772.

Supplemental

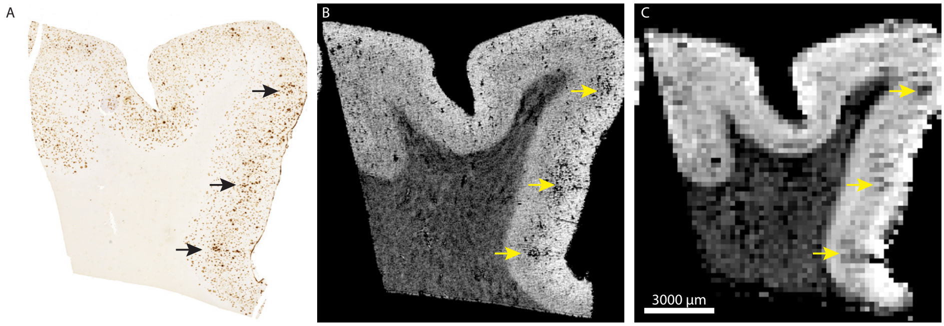

Supplemental Figure 6.1 Cortical hypointense clouds on post-mortem SW images
Examples of "cloud" hypo-intensities (**red arrows**) on the post-mortem low resolution SW images corresponding to Table 6.2 subject 2. These represent a third category of abnormal cortex consisting of diffuse areas with low signal intensity, not extending parallel to the cortical surface but expanding locally in an irregular fashion throughout the cortex.

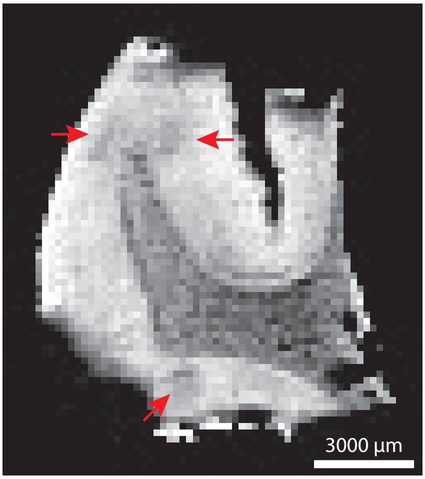

Supplemental Figure 6.2 Focal hypo-intensities on post-mortem SW images
Correlation of Aβ plaques (**A**) with focal hypo-intensities on the post-mortem high (**B**) and low (**C**) resolution SW images corresponding to Table 6.2 subject 4. Similar to previous studies, areas that contain a high amount of large dense core Aβ plaques (*arrows*) typically co-localized with many focal hypo-intensities on the high resolution (isotropic 40 µm voxels) SW images. On the corresponding lower resolution SW images (isotropic 200 µm voxels), however, only some focal hypo-intensities remained discernible, mainly due to partial voluming effects. In general, these focal signal voids contributed to a very small degree to the observed hypointense cortical bands.

Supplemental Table 6.1 Applied immunohistochemistry procedures including primary and secondary antibodies and additional pretreatments

Primary antibody (source)	(dilution)	Secondary antibody	(dilution)	Pre-treatment	Ref.
Anti-human Aβ (6F/3D, DakoCytomation, Glostrup, Denmark)	1:20	#	1:200	†	38
Anti-PHF-tau monoclonal mouse (AT8, Innogenetics, Ghent, Belgium)	1:2000	#	1:200		
Anti-protolipid protein (PLP) monoclonal mouse (Serotec)	1:2000	#	1:200		
Anti-human CD68 monoclonal mouse (KP1, DakoCytomation, Glostrup, Denmark)	1:50	#	1:200	‡	
		¥	1:100	‡	
Anti-human HLA-DR monoclonal mouse (Dakocytomation, Glostrup Denmark)	1:30	#	1:200	‡	
		¥	1:100	‡	
Anti-human GFAP monoclonal mouse (6F2, DakoCytomation, Glostrup, Denmark)	1:1000	# ¥	1:200 1:100	‡ ‡	

Biotinylated rabbit anti-mouse (DakoCytomation, Glostrup, Denmark) followed by ABC (Vector) prior to DAB-enhancement
¥ Goat anti-mouse Alexa Fluor 647 (Invitrogen)
† Formic acid + Trypsin
‡ Steamed for 20 minutes in citrate buffer (pH 6)